

# Atmospheric Water Harvesting Using Thermoresponsive Ionic Liquids

Lainey Ward

*School of Physics, UCD, Dublin*

## ABSTRACT

My four-month project is part of a European investigation into the properties of thermoresponsive ionic liquid/water mixtures in view of application in atmospheric water harvesting. My role involves the analysis of MD trajectories of the ionic liquid [ $P_{4444}$ ][DMBS]. The computations are undertaken in two stages, aiming to characterise the absorption of water vapour at low temperature, and the desorption of water at high temperature, with the former being the primary focus of my project. The simulation results reveal the formation of an outerlayer of IL in the slab in both cases, revealing an interplay between the mixing/demixing transition and surface effects. Nanostructuring is observed in all simulations, and is most pronounced at low temperature. The system's slow kinetics persist at all temperatures, and necessitate the extrapolation of exponential relaxations, including the relaxation times for both the density of water and hydrogen bonds in the slab. A variety of properties regarding the IL slab are estimated, including its surface energy, molecular orientation at the surface, the distribution of electrostatic potential, as well as the distribution of hydrogen bonds. These findings may aid the development of thermoresponsive ionic liquid-based technologies.

## TABLE OF CONTENTS

<b>I. INTRODUCTION</b>	2	1. Water Distribution	8
<b>II. THEORY</b>	2	2. IL Distribution	10
A. Ionic Liquids	2	3. Electrostatic Potential Distribution	11
B. Thermoresponsive Materials	2	4. Water Plastering at the Surface	11
C. Hydrogen Bonding	3	5. Contact Angle	11
D. Water Harvesting	3	6. Surface Energies	12
<b>III. MODEL AND METHOD</b>	3	7. Specific Heat	13
A. Force Fields	3	8. $U_{\text{mix}} + U_{\text{int}}$	15
1. Intramolecular Terms	4	9. Orientation	15
2. Intermolecular Terms	4	C. Stage Two: Water Desorption	15
B. Simulation Method	4	D. Relaxation Relations	15
C. The Simulated Systems	5	1. Water Density	15
1. Stage One: Water Absorption	5	2. Hydrogen Bonding	17
2. Stage Two: Water Desorption	6	<b>VI. SUMMARY</b>	18
<b>IV. ANALYSIS METHODS</b>	6	<b>VII. REFERENCES</b>	19
1. Electrostatic Potential	6	<b>VIII. APPENDIX</b>	20
2. Surface Topography	6	A. Tables	20
3. Surface Energies	7		
4. Interpolation	8		
5. Hydrogen Bonding	8		
<b>V. RESULTS AND ANALYSIS</b>	8		
A. The Dry Slab	8		
B. Stage One: Water Absorption	8		

## I. INTRODUCTION

Providing water to the world's population is a demanding challenge across the globe. There are an estimated 1.1 billion people who lack access to water and 2.7 billion who face water scarcity at least one month a year.<sup>1</sup> Water scarcity can be caused by physical or economic factors, including a lack of infrastructure, altered weather patterns as a result of climate change, and water demand exceeding available resources. The regions most severely affected are landlocked, arid regions, with little precipitation and less developed economies.<sup>2</sup> Many modern harvesting technologies require liquid water sources, electrical input, and sophisticated infrastructures, rendering them unsuitable for such regions. Thus, the development of a water harvesting mechanism capable of extracting atmospheric water under arid conditions remains critical.

This project is devised in accordance with two primary objectives; to investigate ionic liquids (ILs) as a potential water harvesting method, and to evaluate the ability of simulation to characterise this complex process. Regarding the latter, no previous study of this nature has been conducted, and thus it is unknown whether brute force simulation, as used throughout the project, is sufficient to characterise the real-world dynamics of such a system.

My four-month project is part of a comprehensive European computational investigation that began in January 2022 and is expected to conclude in January 2023. The project consists of two stages, concerning: IL-water absorption at low temperature, and IL-water separation at high temperature. During my participation in the project, the former stage advanced significantly. The second stage has only been briefly investigated, but preliminary results are available. Across both stages, my role is to analyse the data generated by the simulated systems for a range of temperatures, water number densities, and simulation times.

## II. THEORY

### A. Ionic Liquids

Ionic liquids are a relatively new class of organic solvents that are typically liquid at temperatures below 100°C. They often comprise organic cations paired with organic or inorganic anions.

ILs exhibit excellent physicochemical characteristics including low volatility, high thermal, high conductivity, non flammability, stability up to 300°C, and ability to dissolve a vast range of organic, inorganic and polymeric compounds.

Although ionic interactions between anions and cations are stronger than the van der Waals forces be-

tween the molecules of ordinary liquids and enhance ordering at all length scales, the low melting point of ILs can be attributed to the relatively large size, flexibility, and low symmetry of their constituent ions. Below 0°C, most ILs are solid-like, being either crystalline or glassy.<sup>3</sup> The glassy state is believed to be only metastable, but may persist down to the lowest attainable temperatures due to the exceedingly slow kinetic of these viscous systems.

The two-component nature of ILs gives rise to an inherent flexibility in design. The vast array of anion-cation combinations enable a great degree of tunability in the design of new materials. In particular, the hydrophobicity of ILs can be fine tuned to promote thermoresponsive behaviour.

These properties establish ILs as an attractive alternative to common molecular organic solvents. For this reason, the study of ILs has expanded to encompass many potential applications such as the extraction of biomolecules, desalination, catalysis, and green chemistry technologies.<sup>34</sup>

### B. Thermoresponsive Materials

Thermoresponsive materials are characterised by a crucial response of their physicochemical properties to changing temperature. In this project, the thermoresponsive material is tetrabutylphosphonium 2,4-dimethylbenzene sulfonate  $[P_{4444}]^+ [DMBS]^-$ , composed of cation and anion pairs. This IL's response to increasing temperature is marked by a reversible transition between a monophasic and a biphasic state.

The monophasic state occurs at lower temperatures and consists of a homogeneous, miscible phase. However, upon heating above a temperature known as the Lower Critical Solution Temperature (LCST), the liquid demixes into its constituents, into the biphasic state. This state consists of a non-miscible IL-rich phase and a solvent-rich phase, separated by a relatively sharp interface, as depicted in Fig. 1. Such phase transitions effectively facilitate the separation and extraction of the constituents of a homogeneous mixture.

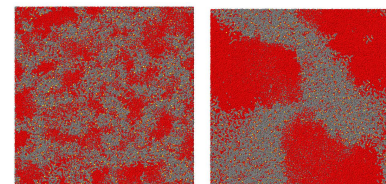


FIG. 1:  $[P_{4444}]^+ [DMBS]^-$  / water solution for  $T < LCST$  (left) and  $T > LCST$  the LCST (right).<sup>5</sup>

Upper Critical Solution Temperature (UCST) ILs behave in a similar nature, however, the liquid transitions into a biphasic state upon cooling below the

UCST. In addition, some thermoresponsive materials exhibit both LCST and UCST behaviour. If a material's UCST>LCST, then the phase diagram is characterised by two distinct curves and if the LCST<UCST, then the phase diagram may appear as a closed-loop, as shown in Fig. 2.<sup>5</sup>

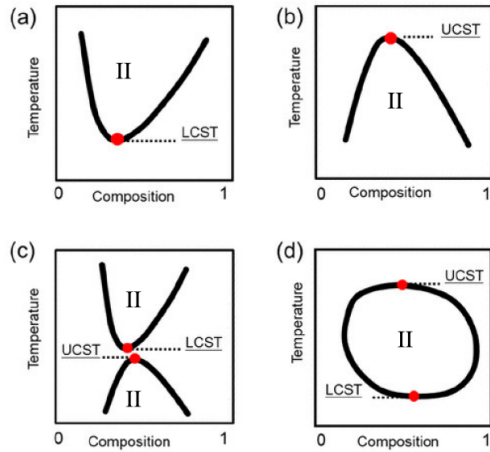


FIG. 2: LCST (a), UCST (b), and combination thermal phase transitions from homogeneous to biphasic states.<sup>5</sup>

The phase-separation temperature of an IL-solvent mixture is dependent on the choice of cation, anion, solvent, and their respective concentrations.<sup>3</sup>

### C. Hydrogen Bonding

As previously stated, thermoresponsiveness arises from hydrophilic and hydrophobic interactions in selected IL compounds. These properties, in turn, are determined by the number and distribution hydrogen bonds (HBs) that link water molecules and ions.

HB, in particular, correspond to specific configurations of triplets of atoms, which consist of two highly electronegative atoms (such as O and N) separated by a hydrogen atom. Bonding occurs through a combination of electrostatic and covalent interactions, and the strength of HBs is not negligible, frequently around 0.5 eV per bond.

Hydrogen bonds are responsible both for the mixing at low  $T$ , since they represent an important source of (potential energy) attraction, and for the demixing at high  $T$ , since the formation of HBs decreases the system entropy due to their short range and directionality. Equivalently, we could say that the breaking of HBs with increasing  $T$  increases the system entropy, decreasing the free energy, and driving the separation of water and ions into distinct parts of the whole system. Therefore, the number of hydrogen bonds in our simulations will reflect the general behaviour of the

entire system, in terms of mixing/demixing.

### D. Water Harvesting

Water harvesting from the atmosphere has the potential to alleviate global freshwater scarcity. The advantage of this technology is that atmospheric water is always available regardless of geographic location, making it a sustainable source of water. However, this technology is particularly advantageous and critical for arid regions, which are frequently landlocked, receive little precipitation, and have few natural bodies of water.

Arid regions typically have a continental climate, characterised by a significant decrease in atmospheric temperature from day to night time. Relative humidity is typically highest at night, reaching up to 50% vapour saturation in desert regions. LCST-ILs exploit such atmospheric conditions through their thermoresponsive phase transition mechanism.

When the atmospheric temperature drops below the LCST during the night, the IL becomes miscible and absorbs water vapour. Conversely, when the atmospheric temperature rises above the LCST during the day, the IL becomes immiscible and separates from the collected water, which may then be harvested. Thus, the IL compound provides a promising means to provide freshwater in arid regions, requiring little or no high quality, expensive energy (electrical power) input, and instead relying on natural heating and cooling to operate.

## III. MODEL AND METHOD

### A. Force Fields

Empirical force fields (FFs) are the fundamental principle on which the study of molecular dynamics is based. A FF is a set of equations and corresponding parameters that characterise the potential energy of a system as a function of its particle's coordinates. In molecular dynamics, the potential in question is the interatomic potential.

Ideally, a FF is sufficiently simplistic to be processed in a realistic time-frame, but sufficiently complex to accurately represent a select region of the true system.<sup>6</sup> Thus, many different force fields have been utilised throughout molecular dynamics, all of varying degrees of complexity. A typical expression for a many-body

interatomic potential is:<sup>7</sup>

$$\begin{aligned}
 U_{\text{total}} = & \sum_{\text{bonds}} \frac{1}{2} k_b (r - r_0)^2 + \sum_{\text{angles}} \frac{1}{2} k_a (\theta - \theta_0)^2 \\
 & + \sum_{\text{dihedral}} \frac{1}{2} V_{\text{proper}} (1 - \cos(n\Phi - \delta)) \\
 & + \sum_{\text{dihedral}} \frac{1}{2} V_{\text{improper}} (1 - \cos(n\Phi - \delta)) \\
 & + \sum_{\text{LJ}} 4\epsilon_{ij} \left( \frac{\sigma_{ik}}{r_{ij}}^{12} - \frac{\sigma_{ij}}{r_{ij}}^6 \right) + \sum_{\text{elec}} \frac{q_i q_j}{r_{ij}}
 \end{aligned} \quad (1)$$

The interatomic potential can be considered in terms of its intra and intermolecular contributions. In Eq. 1, the first four summation terms refer to the intramolecular contributions, and the final two to the intermolecular contributions to the total potential.

To represent a given molecular system, the FF must be parametrised, i.e., the force constants appearing in the general expression of the FF need to be tailored to the actual system. This is done on the basis of the atom types present (H,  $sp^2$  or  $sp^3$  carbon, N, O, P, etc.), and on the type of covalent bonds among them. The parametrisation relies also on ab-initio quantum chemistry computations to assign charges to each atom.

In the present case, the parametrisation has been achieved using a free online service (Automatic topography builder, ATB).

### 1. Intramolecular Terms

The intramolecular terms consist of bond stretching, angle bending and torsions. Bond stretching describes the variation in the length of covalent bonds, and is represented by a simple harmonic potential. Angle bending describes the variation in the angle between the two outer atoms of three sequentially bonded atoms. This is commonly represented as either a harmonic or cosine harmonic potential.

There are two types of torsion potentials in Eq. 1: dihedral angle and improper torsions. Both potentials relate to four bonded atoms: dihedral angle potentials depend on four successively bonded atoms, and improper torsion potentials depend on three atoms bonded to a central fourth atom.

The dihedral angle is the angle formed between the planes of the first and last three atoms. Its potential represents the degree of rigidity of a molecule, and thus has a crucial role in the structure and stability of a system.

The improper torsion is the angle formed between the planes of the central and one outer atom, and the central and two other outer atoms. It is required to maintain planarity and chirality within molecular

structures.<sup>78</sup>

### 2. Intermolecular Terms

The intermolecular terms in the IL's model FF consist of the (12 – 6) Lennard-Jones and Coulombic interactions. The Lennard-Jones energy term refers to both the attractive and repulsive forces between non-bonded atoms. Repulsion occurs due to the overlap of the electron clouds of both atoms. First-principles computations show that this energy depends on distance as a decaying exponential function, however, for the purpose of computational expediency it is assumed to vary as  $r^{-12}$ . Attraction, known as dispersion or van der Waals interaction, occurs due to the correlation between dipoles that fluctuate in time because of quantum zero-point energy. In non-relativistic mechanics, this interaction varies as  $r^{-6}$  ( $r^{-7}$ ).<sup>8</sup>

As already stated, these interactions are often modelled by a Lennard-Jones potential which depends on two parameters;  $\epsilon_{ij}$  is the potential well depth and  $\sigma_{ij}$  is distance at which the potential between two atoms is zero. The computational advantage of assuming the  $r^{-12}$  form for the repulsion energy comes from the fact that this term can be computed as the square of the  $r^{-6}$  term, thus avoiding the (more expensive) computation of an exponential.

The final term accounts for the Coulombic interactions between electric charges.

The computation of intermolecular terms is responsible for most of the CPU time spent in MD simulations. Intramolecular terms and the integration of the equations of motion require only a few percent of the total CPU time (see below).

## B. Simulation Method

Simulations have been carried out using molecular dynamics (MD), integrating numerically the particles' equations of motion:

$$\ddot{\mathbf{r}}_i = \frac{\mathbf{F}_i}{m_i} \quad i = 1, \dots, N \quad (2)$$

where  $\mathbf{F}_i = -\nabla_{\mathbf{r}_i} U_{\text{total}}$  is the force on atom  $i$ , with mass  $m_i$ .<sup>9</sup>

The numerical integration starts from suitable initial conditions  $\{\mathbf{r}_i(t=0); \mathbf{v}_i(t=0)\}$ , in time intervals of 1 fs. Our simulations employ the Verlet integration algorithm.<sup>1011</sup>

The simulation is carried out in the NVT ensemble, meaning that the number of particles ( $N$ ), the system volume ( $V$ ) and the temperature ( $T$ ) remain constant throughout the simulation. Constant (near) zero-pressure is also enforced, as the simulated systems are in contact with vacuum water phase. The

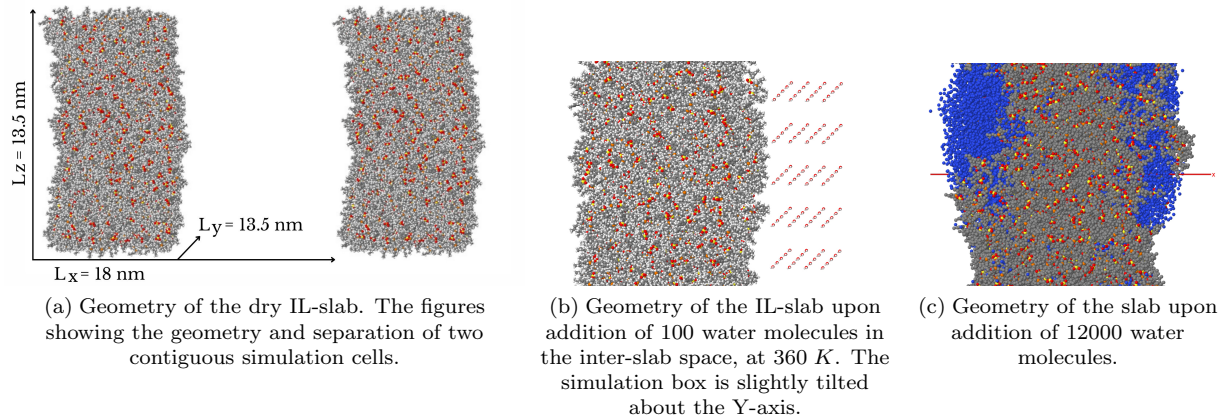


FIG. 3: The simulated systems for Stage One.

constant  $T$  condition is enforced using a Nosé-Hoover thermostat, that relies on a slight modification of the equations of motion.

As in all other slab simulations, the NVT ensemble is used instead of the NPT, due to the presence of free surfaces. If the volume is not fixed, the NPT simulation will reduce the free space, reducing the volume to that of the homogeneous salt/water liquid mixture.

To fully exploit the parallelism of a national supercomputer (Eagle, at Poznan, Poland), simulations have been carried out using the Gromacs package, version 2019.

For each system, the simulation is split into segments 3  $ns$  long, corresponding to  $3 \times 10^6$  discrete integration steps, requiring about 500 core hours (18 hr on 1 node of 28 cores). Trajectories consisting of instantaneous coordinates and velocities are output in a compact form every 100  $ps$ , to be analysed in a later stage.

### C. The Simulated Systems

Simulations have been designed to characterize and quantify the two complementary processes that together carry out water harvesting: low-temperature absorption of water from the vapour into the ionic liquid, and high-temperature separation of water and IL to harvest liquid water.

In both stages, the simulated sample consists of a mixture of water and  $[\text{P}_{4444}][\text{DMBS}]$  where  $[\text{P}_{4444}]^+$  (53 atoms) and  $[\text{DMBS}]^-$  (21 atoms) are shown in Fig. 4.

The  $[\text{P}_{4444}]^+$  cation is rather hydrophobic due to the presence of its hydrocarbons, and has the capability to promote thermoresponsive behaviour with a variety of anions. The  $[\text{DMBS}]^-$  anion is hydrophilic due to the numerous hydrogen-bonding opportunities between water and the  $\text{SO}_3^-$  group of the anion. This balance of hydrophilicity and hydrophobicity gives rise

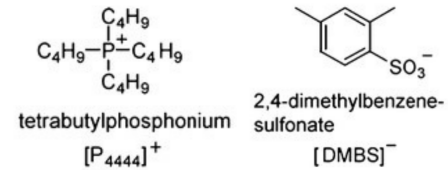


FIG. 4: Structure of the IL compound's constituent cation and anion.<sup>12</sup>

to the thermoresponsive behaviour of the IL, with the compound having an LCST transition at  $T \sim 40^\circ\text{C}$  at 50 – 50 wt% composition.

Below the LCST, the system is nanostructured i.e., characterised by an overall homogeneity, with composition fluctuations corresponding to amphiphatic aggregates rich in IL or water. The presence of these nanostructures might affect the picture emerging from the simulation of finite slabs.

In addition to the LCST, the melting transition must be considered, as it would be unproductive to simulate the system in its solid phase.  $[\text{P}_{4444}][\text{DMBS}]$  does not crystallise, but instead undergoes a glass transition, at a temperature not reported in literature. Similar phosphonium/sulfonate compounds have glass temperatures well below  $0^\circ\text{C}$ , and so it is presumed that the pure IL-samples are liquid-like over the entire temperature range under consideration. However, approaching  $T = 300 \text{ K}$ , the samples become quite viscous.

#### 1. Stage One: Water Absorption

The simulated system is enclosed in an orthorhombic simulation box of sides  $L_x = 18 \text{ nm}$ ,  $L_y = 13.50864 \text{ nm}$ , and  $L_z = 13.50864 \text{ nm}$ , periodically repeated in space. The fixed volume is significantly larger than the equilibrium volume of the system, hence the water and ions will form a slab. On average, the liquid slab is planar, and, to minimise the

surface free energy, it is oriented normal to the longest side ( $L_x$ ) of the simulation box. A 3D configuration of the dry slab at  $T = 360\text{ K}$  is shown in Fig. 3(a).

The slab consists of 1728 neutral ion pairs, with fixed cross section in the YZ plane is  $S_0 = 13.5 \times 13.5\text{ nm}^2$ . The periodicity  $L_x$  along  $x$  is  $18\text{ nm}$ , implying that the slab is separated from its periodic replicas by  $\sim 10\text{ nm}$ , when dry. The relative fraction of empty and filled space can be appreciated in Fig. 3(a), in which the dry slab represents slightly less than half of the simulation box volume. The width of the slab is  $13\text{ nm}$  when covered by 12000 water molecules and so the periodic slab-separation ranges from  $(5 - 10)\text{ nm}$ .

The dry system is prepared by equilibrating the dry slab at  $500\text{ K}$ , and then slowly annealing it to  $T = 360\text{ K}$ . At this temperature, the slab is equilibrated during for a period of  $30\text{ ns}$ , and then annealed again down to the temperatures of interest, i.e., the eleven equispaced temperatures:  $T = (360, 350, \dots, 260)\text{ K}$ . The first batch of 100 water molecules is then added into the vacuum separating two periodic replicas.

For each of these temperatures, water is progressively added in batches of 100 molecules. These molecules are arranged in regular position, forming four layers, removed  $2\text{ nm}$  from the surface of the slab, and  $2\text{ nm}$  from each other. Each layer contains 25 molecules, and forms a square lattice of  $4\text{\AA}$  lattice constant. The initial configuration at  $T = 330\text{ K}$  and  $N_w = 100$  is shown in Fig. 3(c).

Following each addition, the system is equilibrated for  $3\text{ ns}$ . The water vapour is very dilute at all temperatures under consideration, and so the  $3\text{ ns}$  equilibration is sufficient to cause the absorption of the water molecules into the IL, or at least their sticking to the edge of the slab, with only few molecules remaining in the vapour phase. Thus, a subsequent addition of water molecules has negligible probability of overlap with those previously added.

The added water molecules are given random velocities at the beginning of their equilibration, they might end up on either side of the slab, and, before full equilibration, the two water overlays are not necessarily equivalent.

The Stage One computations aim to determine the quantity of water absorbed into the slab as a function of both time and temperature, and to examine the kinetics of water penetration below the surface.

## 2. Stage Two: Water Desorption

The simulations Stage Two begin as a bulk homogeneous, nanostructured sample of 1728 neutral ion pairs and 24000 water molecules, at a 50–50 wt% composition. The slab is initially at  $300\text{ K}$  and re-equilibrated at each of the  $(260, 270, \dots, 360)\text{ K}$  temperatures. To approach the conditions of interest in our study, the

number of water molecules has been reduced, and the side of the simulation box along the X-direction has been increased to that of two nearly parallel free surfaces.

## IV. ANALYSIS METHODS

The output simulation data are analysed using various computations and methodologies, in accordance with theory. The following sections discuss these methods and their underlying theory.

### 1. Electrostatic Potential

On average, the slab in Stage One is homogeneous in the YZ plane. Due to the presence of electrified interfaces within the slab, the charge density along X does not vanish even on average. Rather, it shows oscillations due to the layering of species, parallel to the electrified interfaces. These species not only includes the anions, cations and water, but also their components: the charged cation head, for example.

However, the whole system is neutral. This allows the electrostatic potential across the slab to be computed from the distribution of charge densities along  $L_x$ :

$$V(x) = -4\pi x \int_{x=0}^{x=x} P(x') dx' + 4\pi \int_{x=0}^{x=x} x' P(x') dx' \quad (3)$$

with  $x$ , the position along  $L_x$ , and  $P(x')$ , the charge density at  $x'$ .<sup>1</sup>

### 2. Surface Topography

Topographical data is obtained through the use of a computational method based on Atomic Force Microscopy (AFM). In experiments AFM microscopes, in general, employ a sharp tip to scan across the surface line by line until a three-dimensional surface topography is formed. In the simulation, the time-dependent topography of the IL and water slab along the average plane YZ of the two parallel free surfaces has been characterised by a similar tool, termed virtual AFM (vAFM) for convenience. In the present case, vAFM provides a discretised representation of the surfaces delimiting the distribution of water and ions.

<sup>1</sup> It is easy to verify by differentiation that Eq. 3 satisfies Poisson's equation along  $x$ :

$$\frac{d^2V(x)}{dx^2} = -4\pi P(x) \quad (4)$$

where  $\epsilon_0 = 1$  is implied.

Consider the definition of the two instantaneous surfaces  $\{x_\alpha(y, z), \alpha = \text{left, right}\}$  limiting the slab in any given configuration at time  $t$  along the MD trajectory.

To define the left surface, shown in Fig. 5, a test particle of radius  $r_0 = 2 \text{ \AA}$  is inserted far on the left of the surface, and moved towards the right in small steps  $\delta z$  until it intersects an atom from the slab, whose radius is assigned according to a standard table of Van de Waals radii.<sup>13</sup> If the contact occurs when the centre of the test particle is at  $(\bar{x}, y_i, z)$ , the point identified on the topographical surface is assumed to have coordinates  $\{x_{\text{left}}(y_i, z_i) = \bar{x} + r_0\}$ . The definition of a point on the right surface is analogous, with the obvious difference that the test particle is moved towards the left, and the location of the surface with respect to the contact point is  $\{x_{\text{right}}(y_i, z_i) = \bar{x} - r_0\}$ .

A small but non-vanishing radius  $r_0$  is assigned to the test particle so as to provide a first measure of smoothing, as well as to avoid a systematic overestimation of the slab volume. The determination of a point on the surface takes a small fraction of a second, therefore, it can be undertaken promptly even for many configurations.

The slab surface defined on the discrete grid of  $(y_i, z_i)$  points can be used, for instance, to compute the volume of the slab for various water and IL concentrations or to characterise the roughness of the surface. The approach can also be refined (as it has been done) to quantify the portion of the surface covered by IL or by water, based on the identification of the molecular species giving rise to the contact with the probe particle.

### 3. Surface Energies

Surface free energy, is the excess free energy of a system due to an interface separating two phases at equilibrium. In theory, the surface free energy must be positive, otherwise the systems would spontaneously create new surfaces, for instance splitting into droplets or evaporating. Thus, the surface free energy is analogous to the excess energy created when cutting a bulk sample, creating two surfaces.

Due to the low pressure of the system, the surface free energy is expressed as the Helmholtz free energy (instead of the Gibbs free energy quoted in experiments) as follows:

$$F_s = U_s - T_s S_s \quad (5)$$

with  $U_s$ , the surface potential energy,  $S_s$ , the surface entropy, and  $T$ , the temperature.

Throughout the text, surface energies are referenced as opposed to surface free energies.  $F_s$ ,  $U_s$ , and  $S_s$  have dimensions of energy per unit surface. At room temperature,  $T$  is a small quantity in these dimen-

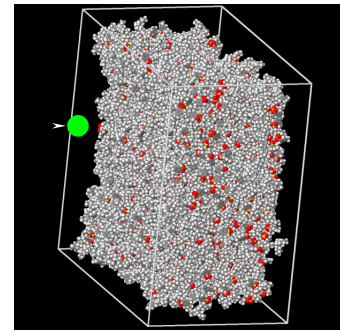


FIG. 5: The left surface and test particle.

sions, and it is presumed that  $S_s$  does not vary significantly between systems. Thus, for the sake of simplicity, surface energies are compared in place of surface free energies. In this project, the systems consist of water-vapour ( $w/v$ ), IL-vapour ( $IL/v$ ), and IL-water ( $IL/w$ ) pairs of surface energies.

The surface energy of simple liquid samples can be computed from the difference in the average potential energy of the slab and of an equivalent amount of the same compound in the extended homogeneous phase.

The surface energy of, for example a pure salt slab is determined as follows:

$$\gamma = \frac{U_{\text{slab}} - U_{\text{bulk}}}{2A_s} \quad (6)$$

with  $A_s$ , the total surface area of the slab's two interfaces under consideration.

The determination of the IL / water interface is less straightforward, because both phases are not pure. In other terms, there is always some mixing of water and IL, even in the demixed state, since the system separates into water-rich and IL-rich phases that do not consist of the pure components. To overcome this problem, we estimate the interfacial energy of IL and water through the contact angle between the water overlayer and the underlying IL surface shortly after deposition, although this state of the system is only a transient.

In our case, the relevant contact angle ( $\theta_C$ ) is angle of the intersection angle between the water liquid-vapour and the IL-liquid water interfaces. The Young equation relates surface energies to contact angle as follows:<sup>14</sup>

$$\gamma_{IL/w} = \gamma_{IL/v} - \gamma_{w/v} \cos(\theta_C) \quad (7)$$

The liquid completely spreads out over the solid at a contact angle of  $\theta_C = 0^\circ$ . Thus,  $\theta_C < 90^\circ$  implies that the solid is hydrophilic, and  $\theta_C$  implies that it is hydrophobic.<sup>15</sup>

I anticipate that the surface properties of our system are determined by the fact that the surface energy of water is high, the surface energy of the IL is low, and

the IL-water interfacial energy is even lower.

#### 4. Interpolation

The specific heat  $c_p$  and  $c_v$ , i.e., the constant pressure and constant energy derivatives of the average potential energy with respect to temperature, tend to be nearly constant. Sharp features in  $c_p$  and  $c_v$  identify essential changes in the system state, such as, for instance, phase transitions. Since these phenomena take place over a narrow interval of temperatures, over broad temperature range the average potential energy tends to depend nearly linearly on temperature.

Surface energies are proportional to the differences of average potential energies, and so they also display a near linear dependence on temperature. Deviations from this linearity are important, and may reveal interesting aspects of results.<sup>16</sup>

To identify such deviations, average potential and surface energies are often interpolated with a function given by the ratio of two polynomials, known as the Padé approximant. A first and second-order Padé approximant are used throughout the analysis, and are as follows.<sup>16</sup>

$$U(T) = \frac{a_0 + a_1 T + \dots + a_{n+1} T^{n+1}}{1 + b_1 T + \dots + b_n T^n} \quad (8)$$

with  $n \geq 1$ .

The degree of the numerator is equal to the degree of the denominator plus one, in such a way that at high temperature, above any phase transition,  $U$  is a linear function of  $T$ . The specific heat  $c_p$  or  $c_v$  can be estimated using the analytic derivative with respect to  $T$  of the  $U(T)$  in Eq. 8.

#### 5. Hydrogen Bonding

In our FF model, hydrogen bonding is defined in purely geometric terms. A HB is recognised when the distance between two electronegative atoms is less than a conventional distance (3.2 Å in our case), and the equilibrium position of the hydrogen deviates by less than 40° from the direction connecting the two other atoms in the bond, as shown in Fig. 6.

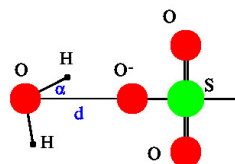


FIG. 6: Schematic of hydrogen bonding between a water and anion molecule.

## V. RESULTS AND ANALYSIS

### A. The Dry Slab

First, a preliminary investigation is made into the structural characteristics and properties of dry  $[P_{4444}][DMBS]$  slabs.

The spatial distribution of the number density of cations and anions are plotted for 360 K in Fig. 7.

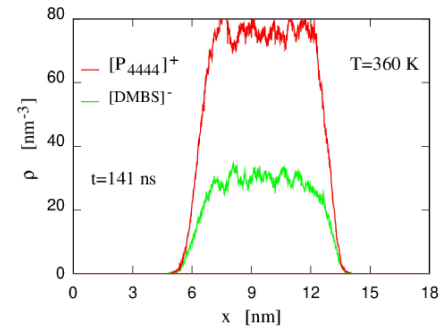


FIG. 7: The number density distribution across the dry slab.

There is found to be no apparent layering of anions and cations at the surface. However, it is revealed that the system has a proclivity for exposing the alkane tail of  $[P_{4444}]^+$  to the vacuum, which is known to have a low surface and free energy. It is determined that the surface energy is particularly low, despite the ionic compound's high cohesion. The calculation of surface energy is undertaken in Section V B 6.

Furthermore, because these alkane tails are hydrophobic, this structural characteristic is unlikely to favour water absorption. Moreover, the system's kinetics appear to be extremely slow, although the addition of water may reduce the sample's viscosity, thereby easing the dynamics.

### B. Stage One: Water Absorption

#### 1. Water Distribution

A wide range of water coverages have been considered and briefly simulated, however, most Stage One computations are concerned the  $N_w = 12000$  sample. Throughout this section, this sample is exclusively discussed.

Water number density and charge density data are acquired for this system, equilibrated for 138 ns at each temperature, and averaged over the last 4 seconds. The water number densities at each temperature are plotted as a function of position in Fig. 8(a).

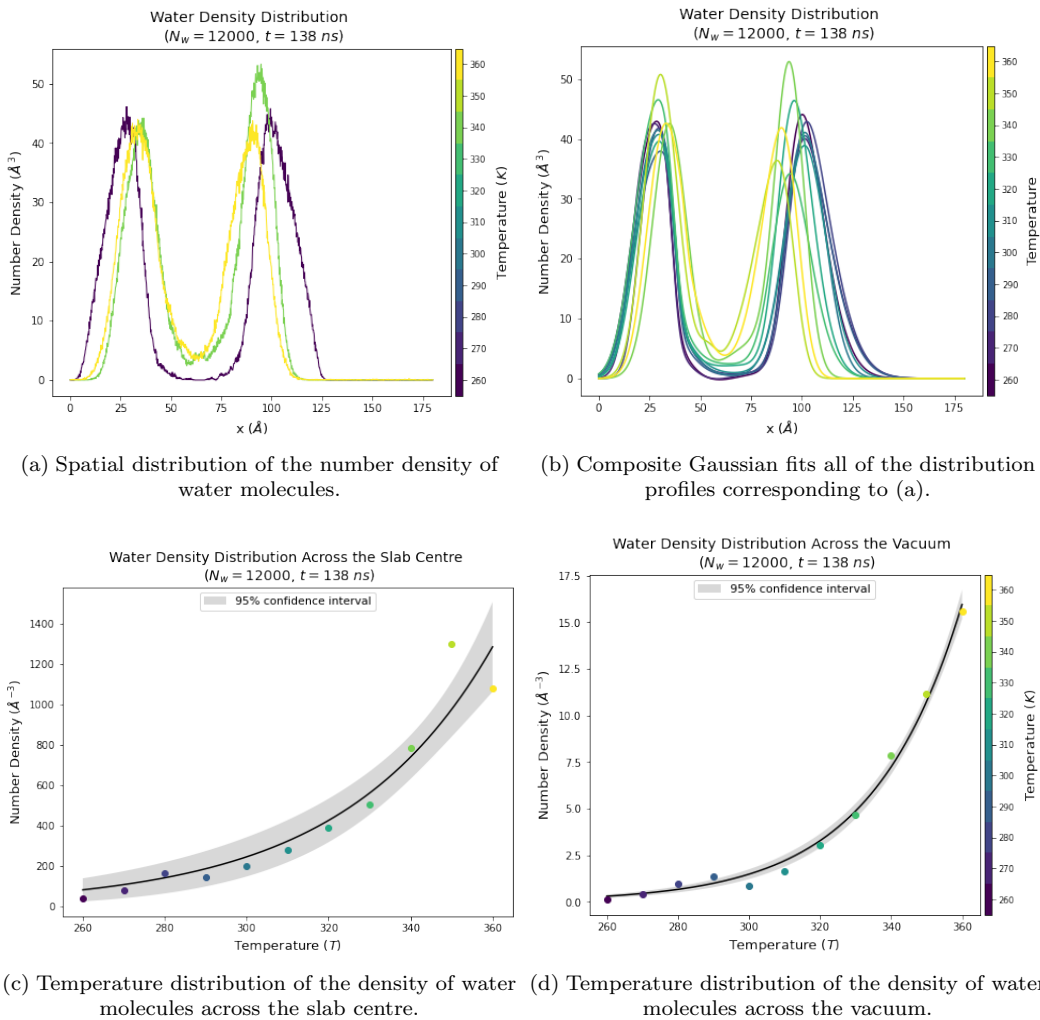


FIG. 8: Water profiles at selected temperatures.

As a consequence of the protocol to prepare samples, adding water to the two sides of the slab, the plots of the water density distribution feature a distinct bi-modal Gaussian distribution. The aim of the simulation is to determine how this initial condition evolves in time, perhaps developing into a single Gaussian distribution across the centre of the slab.

A composite Gaussian model of the water density profile is formed using three skewed Gaussian models, each with four fitting parameters: amplitude ( $A$ ), mean ( $\mu$ ), standard deviation ( $\sigma$ ) and skew ( $\gamma$ ). The model is fitted to the plots and the resulting fits are shown in Fig. 8(b), with parameters listed in Table I. The composite Gaussian model provides a very good fit to the data, with  $R^2 \geq .99$  for all temperatures.

A two-tailed t-test suggests that there is no statistically significant relation between temperature and the distance between the two primary Gaussian peaks, as well as height of either of these peaks, at a confidence level of 95%.

The centre field of the system is estimated to occur in the range  $(50, 70)$ , and the vacuum in the range  $(13.6, 18)$ . The water number density within these regions is plotted as a function of temperature in Fig. 8(c) and 8(d). It is apparent that the total number of water molecules within the vacuum is low across all temperatures, corresponding to a maximum of 0.07% of the system's total water density. Thus, at  $N_w = 12000$  and after  $138 \text{ ns}$ , almost all of the water molecules have successfully penetrated the IL-slab.

The plots for both regions have been fitted to an increasing exponential function using an explicit Orthogonal Distance Regression (ODR) model. The models provide a very good fit to the data with  $R^2 \geq .98$  in both regions. Thus, both the number of water molecules penetrating the centre of the simulation box and remaining within the vacuum increases exponentially with temperature.

Using a 3D configuration of the system, the distribution of water parallel to the surface is examined, see

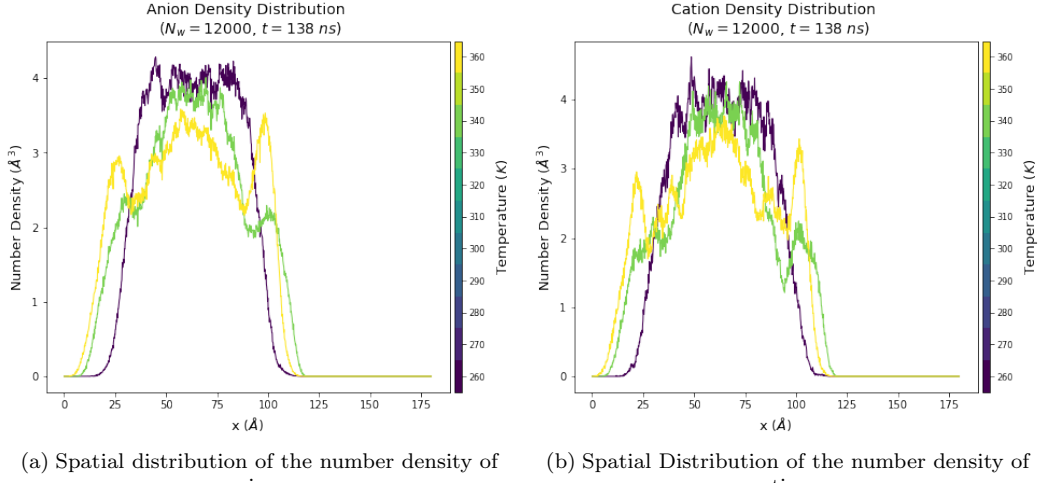


FIG. 9: IL profiles at selected temperatures.

Fig. 8. It is apparent that water forms nanometric droplets, separated from one another. The geometric structure of a singular droplet is further examined in Section V B 4.

## 2. IL Distribution

Cation and anion number density data are also acquired for the same system in the previous section. The cation and anion number densities at each temperature are plotted as a function of position in Fig. 9. Each of the profiles feature a noisy peak that plateaus across the slab centre, corresponding to the region in which the number density of water molecules is minimised. The cation and anion profiles evolve analogously with increasing temperature, with local extrema emerging at approximately the same positions due to ionic bond shared by the anions and cations.

At  $T > 300\text{ K}$ , the central peak of the profiles narrows and two smaller peaks emerge on either side. The entire distribution broadens at the edges of the slab, at which the cations form a thin layer beyond the anions. Both effects become more pronounced at increasing temperatures.

A more thorough understanding of the system can be obtained through cross-analysis of the water and IL distributions. These are overlaid in Fig. 12 for the highest and lowest simulated temperatures.

At the lowest temperature, the system is primarily characterised by two pairs of interfaces; vacuum-water and water-IL. At the highest temperature, the IL distribution has extended beyond that of water, forming a new outermost molecular layer. Water occurs in the first interlayer between the outer and inner IL layers. Thus, three pairs of interfaces are now formed; vacuum-IL, IL-water, and water-IL.

This systematic change is also apparent from the 3D configuration of the system, as shown in Fig. 10. This features ions crawling above and across the water surface, at the higher temperature.

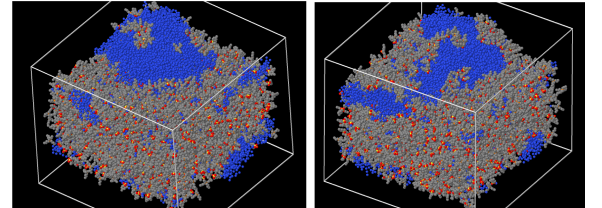


FIG. 10: Configuration demonstrating the progressive layering of ions above the water surface from  $T < \text{LCST}$  (left), to  $T > \text{LCST}$  (right). The cation's hydrocarbon tails appear in grey.

This layering phenomenon occurs as it promotes a decrease in the surface free energy of the slab at higher temperatures, giving rise to a more stable configuration. This can be understood in terms of the bulk surface energies associated with each configuration. Assuming a model under which the IL and water are immiscible, the two-pair interface system has a combined surface energy of:

$$\gamma_{\text{tot}} = 2(\gamma_{w/v} + \gamma_{w/IL}) \quad (9)$$

For the three-pair interface system this becomes:

$$\gamma_{\text{tot}} = 2(\gamma_{IL/v} + 2\gamma_{IL/w}) \quad (10)$$

Thus, the surface energy of the latter is less than the former if  $\gamma_{w/v} > \gamma_{IL/v} + \gamma_{IL/w}$ . This is shown to be true in Section V B 6, using computed surface energy values. As mentioned, the low value of  $\gamma_{IL/v}$

is attributed to the tendency of the IL to expose its alkane tails towards the vacuum. At the same time,  $\gamma_{IL/w}$  is decreased by orienting  $P^+$  towards water.

### 3. Electrostatic Potential Distribution

The charge densities at each temperature are plotted as a function of position in Fig. 11(a). These have been symmatrised with respect to a fixed centre, determined on the basis of the cation and anion densities. The plots appear significantly noisy within the range of the simulation box, and the range of charge densities tend to decrease with increasing temperature.

The system potential is determined from the charge density profile in accordance with Eq. 3 in Section IV 1, and is plotted as a function of position in Fig. 12. Within the simulation box, the potential profiles feature a central maximum with a minimum to either side.

The potentials do not converge to 0 where  $x > 150 \text{ \AA}$  simply due to an imbalance in the symmetrisation of the charge densities.

The analysis of local extrema using a two-tailed t-test reveals many systematic, statistically significant linear relations. There is a strong correlation between the potential at the central maximum and temperature ( $r = -.89$ ,  $p < .05$ ).

Furthermore, there is a very strong correlation between the distance between the minima and temperature ( $r = -.90$ ,  $p < .05$ ), as well as between the potential at these minima and temperature, ( $r_L = -.86$ ,  $p_L < .05$ ) and ( $r_R = -.59$ ,  $p_R < .06$ ). Therefore, generally, as temperature increases, the minima become closer together and the average potential within the centre field decreases.

Again, a more thorough understanding of the system can be gained from cross-analysis of the water number density and potential distributions overlaid in Fig. 12. Across all temperatures, there is a mean distance of  $\sim 1.7 \text{ nm}$  and  $2.5 \text{ nm}$  between the two leftmost extrema, and the two rightmost extrema of the water number density and the potential plots. Thus, the positions at which water density is highest, are highly correlative with those at which the system potential is lowest. The converse is also true, indicating that the electrostatic potential distribution somewhat mirrors that of water. This can be attributed to the formation of electrified interfaces.

### 4. Water Plastering at the Surface

In accordance with the method discussed in Section IV 2, topography data of the slab's upper surface are acquired for the system containing 12,000 water molecules, equilibrated for  $32 \text{ ns}$ , and averaged over the last 4 seconds. A 3D surface profile of the data is

shown in Fig. 13(a). The water droplet under consideration occurs in the centre region of the plot, and is surrounded by smaller pronounced surfaces. Note that the  $Z$  axis appears exaggerated, and the droplet is, in actuality, spread rather flat across the slab surface.

The ranges of X- and Y- coordinates over which these noisy segments occur are visually determined and their corresponding Z-coordinates and disregarded in further analysis. The resulting noise-reduced singular droplet surface is shown in blue in Fig. 13(b).

It is apparent that the droplet is irregular in both height and spread. Although the droplet's features four trailing arms in the XY plane, it is generally parabolic in shape. For this reason, a paraboloid function is fit to the data using an Orthogonal Distance Regression model as follows:

$$Z = f(x, y) = Ax^2 + By^2 + Cxy + Dx + Ey + F \quad (11)$$

with fitting parameters A, B, C, D, E, and F, given in Table II.

The model fits moderately well to the data, indicated by an  $R^2$  value of 0.75.

### 5. Contact Angle

As discussed in Section VB 6, the surface energies of the system can be estimated using the droplet's contact angle. Using the paraboloid model in Eq. 11, a 2D cross section through the focus, parallel to the Y-axis, is produced. The spatial resolution is increased to 1000 data points and the X-range is set so as to ensure interception with IL-surface plane.

The data is significantly linear in the range of  $\sim 200$  data points across each of the two intercepts ( $r > .99$ ,  $p < .05$ ) and so a linear ODR model is fit to the parabola, within this region.

The contact angle formed between the linear function and the basis plane is:

$$\theta = \tan^{-1} (|m|) \quad (12)$$

with  $m$ , the slope of the linear function.

This process is also undertaken for a 2D cross section of the paraboloid, parallel to the X-axis. The best-fit parameters of the four linear functions and their corresponding contact angles are listed in Table III. The linear functions provide an excellent fit with  $R^2 > .99$  in all instances.

The mean angle corresponding to each parabolas differ by a mean of  $\sim 3^\circ$ , and the overall mean angle is taken as  $(34 \pm 3)^\circ$ . This value implies that the IL slab surface is hydrophilic, and reinforces that the water droplet is quite flat and high wetting occurs.

Taking this contact angle and Eq. 7, the surface en-

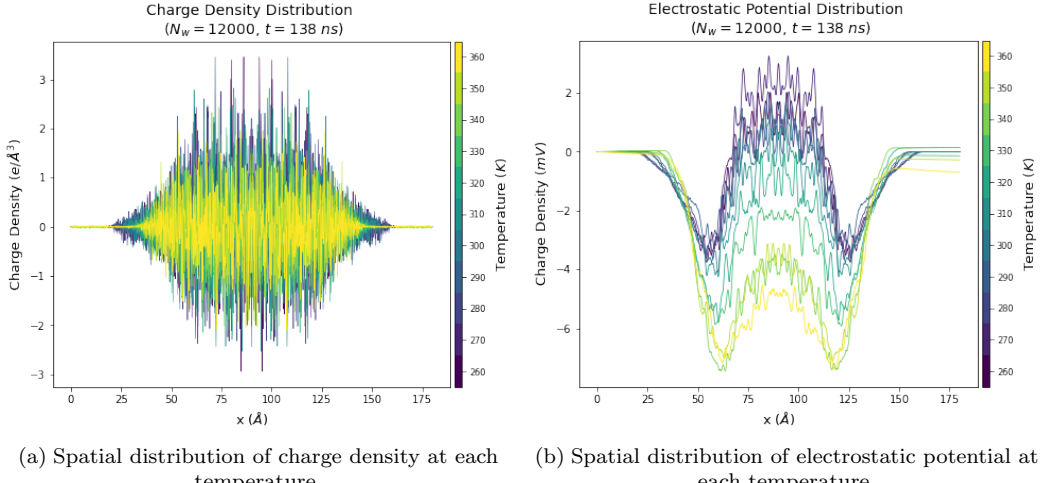


FIG. 11: Symmetrised charge density and electrostatic potential profiles.

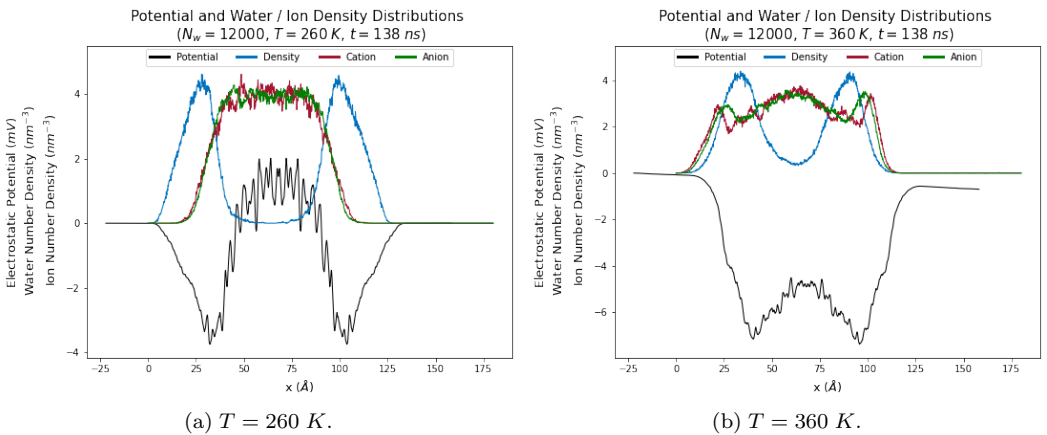


FIG. 12: Combined density and electrostatic potential profiles.

ergies between the droplet-vapour-IL interfaces are related as follows:

$$\gamma_{IL/w} = \gamma_{IL/v} - (0.83 \pm 0.03) \gamma_{w/v} \quad (13)$$

The uncertainty on the angle could be reduced using a more quantitative method to average  $\theta_C$  across the paraboloid, as well as through analysis of multiple droplets within the same system.

Values for  $\gamma_{w/v}$  and  $\gamma_{IL/v}$ , and thus  $\gamma_{IL/w}$  are computed in the following section.

### 6. Surface Energies

Average potential energy data is obtained for various samples, at each temperature in the given range. These samples include: the salt slab, bulk salt, water slab, water bulk, and the hydrated slab.

The salt slab has a cross section of  $\sim 13.51^2\text{ nm}^2$ ,

and is composed of 1728 ion pairs. The bulk salt is computed as the average potential energy of a homogeneous system with the same number of ion pairs.

The water slab has a cross section of  $13.31^2\text{ nm}^2$ , and is composed of 86400 water molecules. The bulk water is also computed as the average potential energy of a homogeneous system with 200000 ion pairs.

The hydrated slab has the same cross section as the salt slab, and is composed of 12000 water molecules and 1728 ion pairs. The hydrated bulk is computed from a homogeneous sample of the same composition.

The surface energy of pure water is computed from the energy difference between the water slab and bulk using Eq. 6. The resulting plot is shown in Fig. 14(a). Similarly, the surface energy of pure IL is computed from the energy difference between the salt slab and bulk and is shown in Fig. 14(b). The surface energy of the salt is low compared to that of water. This is surprising as the cohesive energy of the salt is much

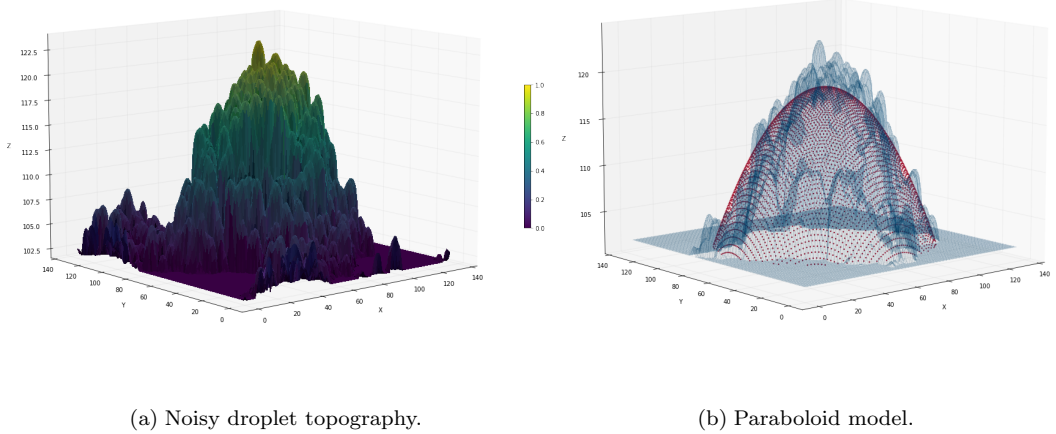


FIG. 13: Water droplet profiles.

higher than that of water. This anomaly can be attributed to the layering of salt at the surface, in which the orientation of the salt's hydrocarbon tails and moiety effectively decrease the IL slab's surface tension.

The surface energy of the pure hydrated slab is computed with respect to the separated salt and water bulk, as well as to the hydrated bulk. These are plotted in Fig. 14(c) and 14(d). As Eq. 6 is inversely proportional to  $A_s$ , the  $0.20^2 \text{ nm}^2$  difference in cross section between the salt and water slabs is assumed to be negligible.

The surface energy of the hydrated slab relative to the mixed bulk tends to be high, especially at low temperatures when the slab is not well equilibrated.

The surface energy of the hydrated slab relative to the separated salt and water bulk is consistently lower than both the pure salt and water surface energies. This may be attributed to the different methods of preparation of the bulk and hydrated samples. The homogeneous samples are prepared at each temperature by decreasing the temperature from  $360 \text{ K}$  in increments. Therefore these samples are well mixed and have higher potential and surface energies. However, the hydrated samples are prepared independently at each temperature, and feature water condensing on the slab surface; a thermodynamically different system to the homogeneous samples. This has resulted in the samples being less well mixed, and thus they have lower potential and surface energies than if they had have been prepared using the same method as the homogeneous samples. Therefore, the energy disparity between the homogeneous and hydrated samples should be attributed to a bulk energy, as opposed to a surface energy.

$\gamma_{\text{IL}}$  is computed from Eq. 7, and plotted as a function

of temperature in Fig. 14(e). The water / IL surface energy is negative, indicating that the IL slab and water molecules are mixed.

The five aforementioned surface energy plots are each fitted to a Padé approximant. The surface energy plots for water, the hydrated slab relative to the separated bulk, and water / IL are fitted to a first-order Padé approximant, and the plots for the salt and the hydrated slab relative to hydrated bulk are fitted to a second-order Padé approximant. In the instances where it is unclear whether a first or second-order fit is most suitable, for example, in the salt surface energy plot, a one-way Chi-squared goodness of fit test is performed for both order approximants. This tests the null hypothesis that there is no significant difference between the data and approximant fit. Provided both p-values lie within the 5% significance level, the approximant with the lowest corresponding chi-squared statistic is selected as the most appropriate fit.

The approximants provide an excellent fit to the data, with all five having  $R^2 > .860$ .

## 7. Specific Heat

The derivative of the surface energy, the specific heat at (near) constant pressure, of the hydrated slab relative to the hydrated bulk is plotted as a function of temperature in Fig. 14(g). A second-order Padé approximant is fitted to the data. The local minimum of the plot occurs at  $\sim 313 \text{ K}$ , in close proximity to the LCST at  $313.2 \text{ K}$ .

As discussed in Section IV 4,  $c_p$  should form a near linear and positive dependence with temperature. Therefore, this minima cannot be attributed to the system's LCST phase transition, but rather progressively

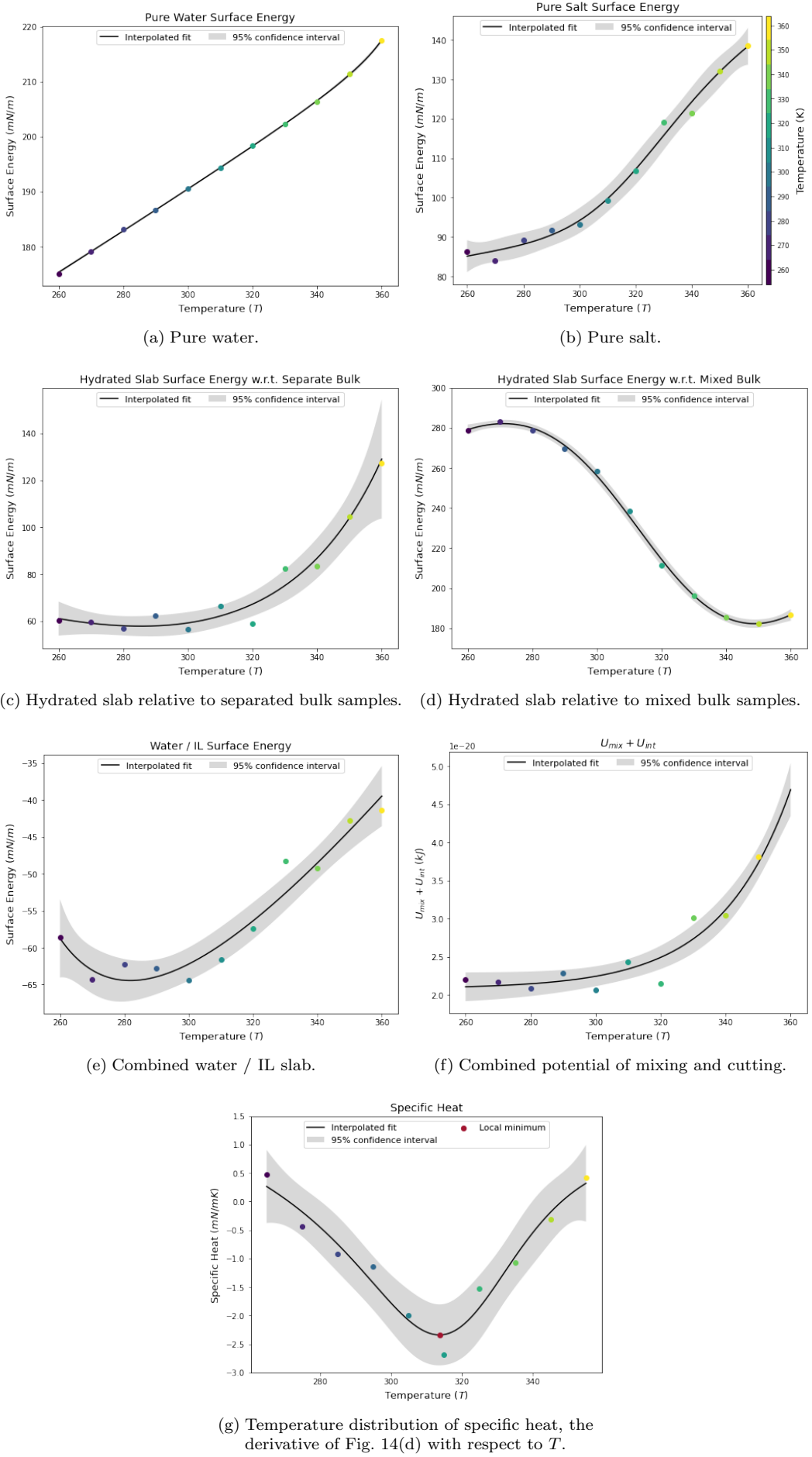


FIG. 14: Surface energy profiles. Each figure is fitted to a Padé approximant.

poor equilibration in decreasing  $T$  to low temperatures.

### 8. $U_{\text{mix}} + U_{\text{int}}$

The addition of the interfacial and mixing potential energies is given as follows:

$$U_{\text{mix}} + U_{\text{int}} = U_{\text{tot}} - U_w - U_{\text{IL}} \quad (14)$$

$U_{\text{mix}}$  is computed using the data from the previous section and is plotted as a function of temperature in Fig. 14(f). Again, a Padé approximant is fitted to the data, with fitting parameters listed in Table V.

### 9. Orientation

The number density distribution of  $P^+$  atoms and entire cations is shown for the dry slab in Fig. 15(a), and also for the hydrated slab in Fig. 15(b), both at 141  $ns$  and 360  $K$ . The density of  $P^+$  is scaled for the purpose of visualisation.

It is apparent that the density distribution of  $P^+$  is slightly narrower than that of the entire cation, particularly at the edges of the slab. Moreover, in the hydrated case, the  $P^+$  distribution begins at the same position as the water distribution. This implies that the  $P^+$  is hydrophilic, which is anticipated as  $P^+$  tends to be screened by water. This, in turn, implies that the cation's alkane tails are oriented towards to vacuum.

## C. Stage Two: Water Desorption

As discussed, so far Stage Two has been investigated to a much lesser degree than Stage One. The number density of water, anions and cations are shown in Fig. 16, for 260  $K$  and 360  $K$ , at a simulation time of 50  $ns$ .

It is apparent that at the lowest temperature, the components are in fact mixed across the slab. However, following the increase of  $T$  above the LCST the IL forms an outermost layer, around a bulk of both water and IL. Examination of the 3D configuration of the system, shown at 360  $K$  in Fig. 16(c), reveals that the water and IL are phase separated within the bulk, with the IL forming a thin layer around the slab. This layering is attributed to the same surface effects observed in the simulation of water absorption.

The bulk simulations from which the initial samples have been taken, show a clear demixing transition from a nanostructured system at  $T < 310 K$  to a demixed state at  $T > 310 K$ . The transition is not very sharp, therefore the transition temperature is somewhat uncertain.

Once the water / IL are demixed, the water may be harvested by exploiting the different densities of water

and IL, for instance, by centrifugation of mild pressure filtration through a porous membrane.

## D. Relaxation Relations

### 1. Water Density

The simulations thus far show that the kinetics of both the dry and hydrated slabs are exceedingly slow. This limits the ability of the MD to provide a reliable view of the system's equilibration properties within the short duration of my project. While the overall project is still ongoing and further simulations will solve most of the time scale problem, I discuss here an approach to extrapolate results from a simulation of limited duration to longer time scales. A variety of statistical mechanics methods such as accelerated sampling approaches (metadynamics, Markov state models, etc.) are in use to this aim, but I explored a simpler approach based on the peculiar properties of the system and the process under investigation.

The protocol for the system preparation, which involves the progressive addition of water, implies that the initial system is significantly out-of-equilibrium. However, over time, the system and its properties will slowly relax to their equilibrium states. Under these conditions, the statistical mechanics analysis shows that the time evolution of the systems consists of fast fluctuations, superimposed to longer time relaxation processes, whose time dependence is primarily exponential.<sup>171819</sup>

Thus, provided the fast fluctuations are averages out or removed by some appropriate method, any collective property of the system will display a time dependence that can be expressed as the sum of decaying exponential terms.

As an example, I discuss the relaxation of the density of water in the centre of the slab ( $50 \leq x \leq 70$  Å), investigated for the system containing 12000 water molecules. This property is plotted as a function of simulation time in Fig. 17, for 320  $K$  and 360  $K$ .

Since the time dependence of this property is presumed to be exponential, the density distribution plots are fitted by the sum of exponentials as follows:

$$\langle \rho \rangle(t) = \langle \rho \rangle(\infty) + \sum_i c_i \exp(-t/\tau_i) \quad (15)$$

with fitting parameters  $\langle \rho \rangle(\infty)$ ,  $c_i$ , and  $\tau_i$ , and the sum extends over a number of different terms.

In principle, a large number of terms could be used to achieve a nearly exact fit, however, the fit would then become poorly conditioned. Thus, both temperature plots are fit to a sum of two exponential terms only, intended to identify the major relaxation modes of the system. Extrapolation of the fit to long times

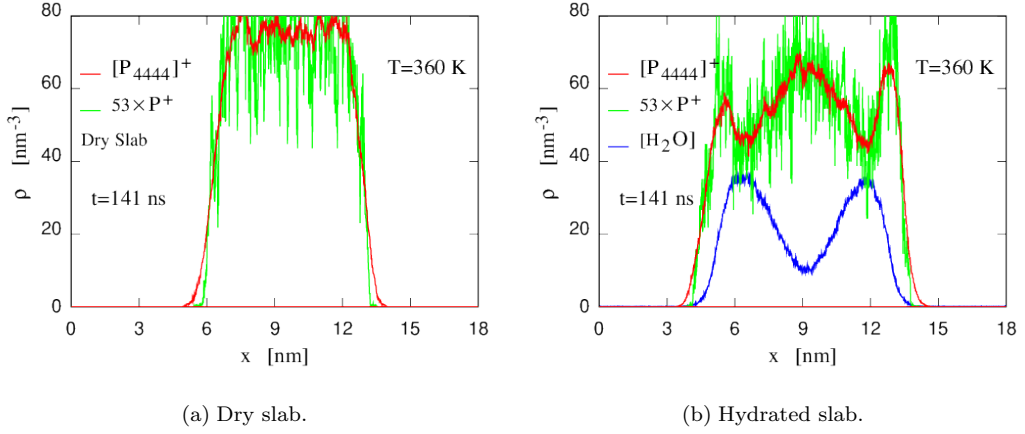


FIG. 15: Spatial distribution of the number density of  $P^+$ , cations, and water at 360 K.

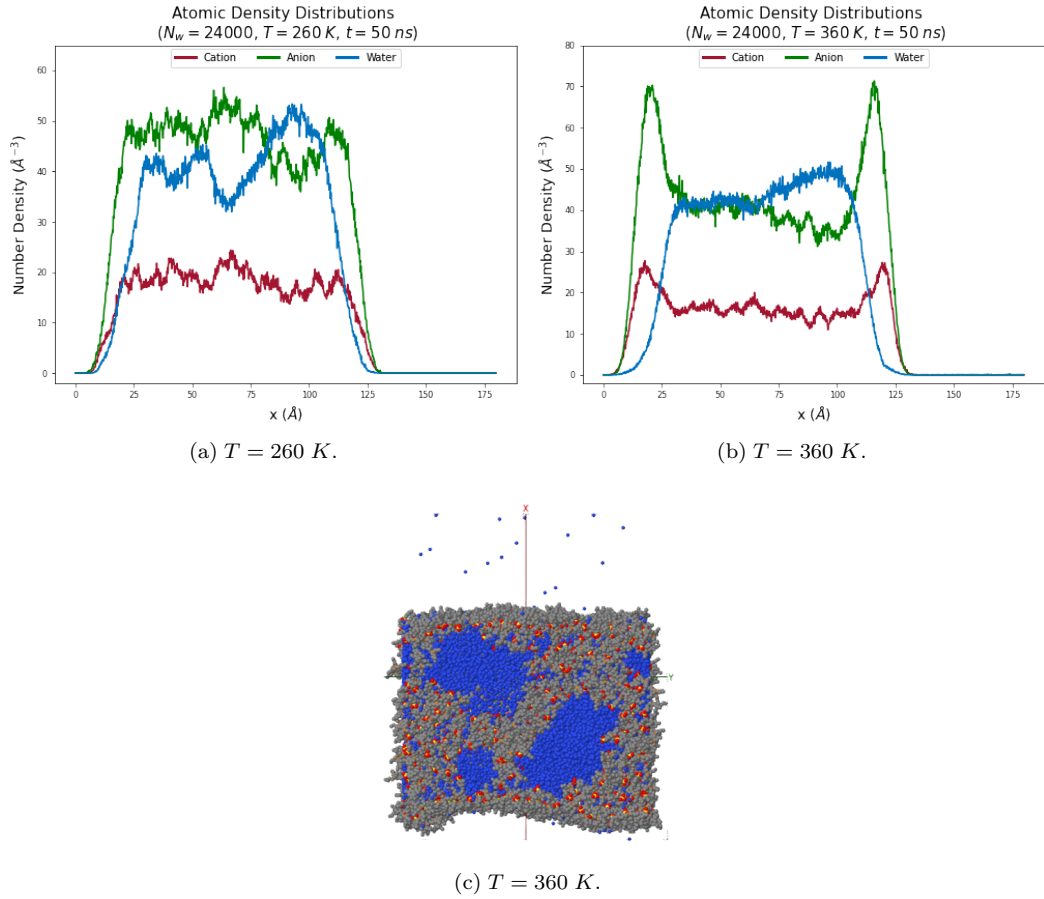


FIG. 16: Spatial distribution of number density profiles in Stage Two. The density of each ion profiles totals to the number of anion and cation-associated atoms (21:53), rather than the total number of ions (1:1).

allows to predict the asymptotic value of the collective variable.

At  $T = 360$  K the asymptotic value is  $30 \text{ nm}^{-1}$ , approximately three times greater than the highest value measured during 140 ns of the simulation. Interest-

ingly, the asymptotic value of at  $T = 320$  K has a comparable value of  $28 \text{ nm}^{-1}$ .

It is also apparent that the system relaxes its water density profile through a fast ( $\tau_1$ ) and a slow ( $\tau_2$ ) channel. The total relaxation time quoted in the figures is

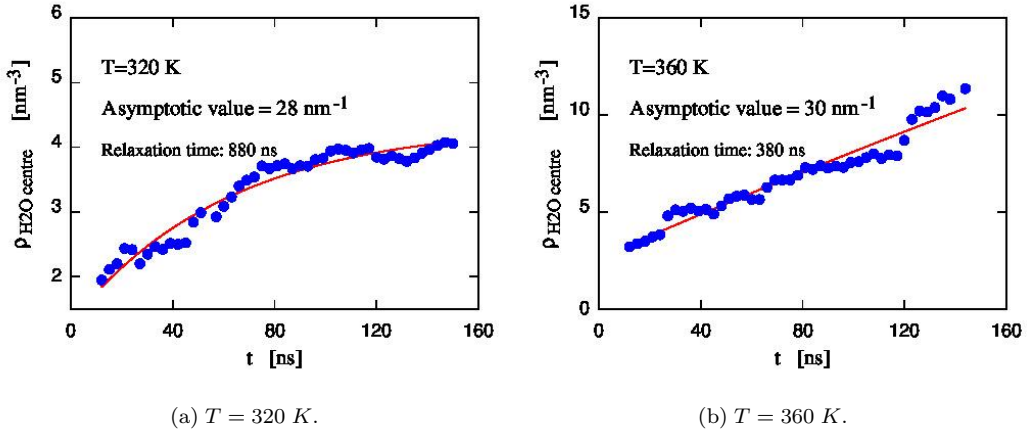


FIG. 17: Time evolution of the average number density of water molecules across the slab centre.

taken as the geometric mean of the two characteristic times, and is over two times greater at  $T = 320$  K than at  $T = 360$  K, with a value of 880 ns.

A first check of consistency of the method is its stability with respect to the addition/subtraction of data in the set used to obtain the exponential parameters. I verified that progressively adding data provided by new simulation runs does not affect significantly the predictions of the extrapolation.

Evidently, this approach has yielded promising results. Needless to say, further testing is required to validate this approach, including comparisons to longer simulations and standard accelerated sampling schemes.

## 2. Hydrogen Bonding

Data for the number of HBs in the slab are determined for the system of 12000 water molecules in accordance with Section IV 5. The number of HBs is plotted as a function of simulation time in Fig. 18, in which each data point has been averaged over 3 ns.

It is apparent that, in a similar nature to the density of water molecules in the slab, the number of HBs also begins in an out-of-equilibrium state and slowly relaxes to equilibrium. A composite model of two decaying exponentials is fitted to the data, again, representing a fast and slow relaxation channel.

At  $T = 320$  K, this relaxation time is 972 ns, which is comparable to that of 880 ns for the density of water molecules in the slab centre, at the same temperature. The asymptotic value corresponds to approximately 1 HB per anion, indicating that the system becomes predominately demixed. This corresponds to more than one water molecule per ion pair, however, not every water molecule is bonded to an anion.

Therefore, the IL-rich phase contains almost no wa-

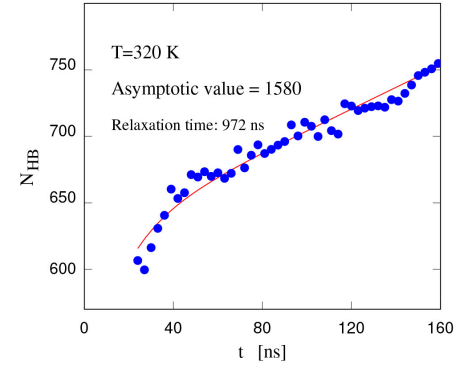


FIG. 18: Time evolution of the number density of HBs at 320 K.

ter, however, the IL-rich phase contains about 10 wt% of water.

Analysis of the simulations over the temperature range reveals that water and anions form a multitude of HBs at low  $T$ , and this number decreases steadily up to the LCST. Above this point, the number of water-anion HBs drastically reduces, but does not vanish, since the IL-rich phase still contains about 10 wt% of water at equilibrium. The number of water-anion HBs cannot be estimated as a function of  $T$  as the slow relaxation at low  $T$  prevents a reliable fit to the simulation data.

## VI. SUMMARY

During the four months of my project, I have been a part of a European team investigating the properties of thermoresponsive water / IL mixtures in view of energy and environmental applications in water desalination, permanent storage of heat, and water harvesting from the atmosphere. My task has been to analyse the trajectories generated by the MD simulations in order to investigate the process of water harvesting from the atmosphere using thermoresponsive ILs. The approach, proposed by Forero-Martinez et al. (2021), is based on the absorption of water at the relatively low temperature of the night, and on its desorption at the high temperature of the afternoon, exploiting the wide temperature oscillation typical of arid, landlocked regions.

Water absorption and desorption occur through the surface of the IL, hence the simulation concerned a slab of IL, confined by two parallel planar surfaces. Moreover, the two stages of low temperature absorption and high temperature desorption have been investigated separately. The IL considered in the computational study has been  $[P_{4444}][\text{DMBS}]$ , whose structure and properties have been briefly discussed in the introduction. Samples, in particular, consisted of 1728 ion pairs, and up to 12000 water molecules.

The computational plan which my project has been a part of spans more than one year, and is not yet in the middle of its duration. Therefore, my project cannot report conclusive results, but rather focuses on the system, the simulation method, and, in particular, the analysis of simulation trajectories. Although preliminary, the results are already interesting, and point to important properties that are relevant to water harvesting applications.

In a preliminary stage, the properties of dry  $[P_{4444}][\text{DMBS}]$  slabs have been investigated. Analysis of the slab's thermodynamic properties and surface structure reveals that, despite the ionic compound's high cohesion, the surface energy is particularly low. This owes to the system's proclivity for exposing the alkane tail of  $[P_{4444}]^+$  to the vacuum, which is known to have a low surface and free energy. Because these alkane tails are hydrophobic, this structural characteristic is unlikely to favour water absorption.

Water absorption has been investigated by progressively adding water to the dry sample, until a coverage of 12000 water molecules was achieved. The simulation of this water / IL system has accounted for the majority of computations (until now). The MD results, which span approximately 150  $ns$  of simulation time, demonstrate the interplay between the mixing/demixing transition driven by bulk thermodynamics, and the strong surface effects arising from the contrasting surface properties of water and  $[P_{4444}][\text{DMBS}]$ . For instance, the high surface energy

of water and the low surface energy of  $[P_{4444}][\text{DMBS}]$ , combined with the low IL-water surface energy, determine the peculiar layering at the slab's surface. The surface tends to be covered by a thin IL film even when the bulk thermodynamics imposes a full separation of water and IL.

To a lesser extent, water desorption has been investigated using a homogeneous, nanostructured, and hydrated sample. The MD results span 50  $ns$  of simulation time and are attained for a temperature of 360  $K$  only. Again, there is a full separation of water and IL within the bulk, followed by the formation of a thin IL film at the surface. This layering is attributed to the same surface effects observed previously. This water may be harvested by exploiting the different densities of water and IL. Therefore, despite the limited simulations, the results indicate that desorption at high temperature is a viable process.

Furthermore, nanostructuring, defined as the formation of domains of nanometric size composed primarily of water or IL, is observed in all absorption and desorption samples, and is most pronounced at low temperatures, as anticipated.

Simulations also show that the dry slab's slow kinetics persist even after the addition of water to the slab. Together with the my project's limited duration, this has motivated the exploration of methods to extrapolate results from a simulation of limited duration to longer time scales. In the case of water density in the slab centre and the density of HBs, this relaxation is dominated by two primary relaxation channels, both presumed to be decaying exponentials. This approach has been tested in practice and has yielded promising results. Of course, further testing is required to validate this approach.

Apart from these major findings and considerations, the analysis of the MD trajectories has revealed a variety of microscopic details about the structure and properties of the  $[P_{4444}][\text{DMBS}]$  samples, including, for instance, their surfaces energies and molecular orientation at the surface, the profile of electrostatic potential across the slab, as well as the number and distribution of hydrogen bonds linking water and ions. All these properties have been briefly discussed in the report, and it is likely that their clarification and understanding will aid the development of thermoresponsive ionic liquid-based technologies.

## VII. REFERENCES

- <sup>1</sup> A. Y. Hoekstra *et al.*, “Global monthly water scarcity: Blue water footprints versus blue water availability,” *PLoS One*, vol. 7, no. 2, pp. 1–9, 2012.
- <sup>2</sup> F. Rijsberman, “Water scarcity: Fact or fiction?,” *Agricultural Water Management*, vol. 5, no. 22, pp. 5–22, 2005.
- <sup>3</sup> T. Cremer, *Ionic Liquid Bulk and Interface Properties: Electronic Interaction, Molecular Orientation and Growth Characteristics*. Nuremburg: Springer International Publishing, 2015.
- <sup>4</sup> B. Paul and S. Moulik, *Ionic Liquid-Based Surfactant Science*. New Jersey: John Wiley Sons, 1 ed., 2013.
- <sup>5</sup> N. C. Forero-Martinez, R. Cortes-Huerto, A. Benedetto, and P. Ballone, “Thermoresponsive ionic liquid/water mixtures: From nanostructuring to phase separation,” *Molecules*, vol. 27, no. 5, pp. 1647–1694, 2022.
- <sup>6</sup> M. González, “Force fields and molecular dynamics simulations,” *PLoS One*, vol. 12, no. 1, pp. 169–200, 2011.
- <sup>7</sup> PumMa, “Potentials,” 2007.
- <sup>8</sup> D. Rapaport, *The Art of Molecular Dynamics Simulation*. New York: Cambridge University Press, 2 ed., 2004.
- <sup>9</sup> J. Junquera, “Molecular dynamics in the microcaconical (nve) ensemble: the verlet algorithm.”
- <sup>10</sup> D. Frenkel and B. Smith, *Understanding Molecular Simulation*. San Diego: Academic Press, 2 ed., 2003.
- <sup>11</sup> U. Schiller, “An overview of integration schemes for molecular dynamics simulations,” *Max Planck Institute for Polymer Research*, 2008.
- <sup>12</sup> Y. Kohno and H. Ohno, “Temperature-responsive ionic liquid/water interfaces: relation between hydrophilicity of ions and dynamic phase change,” *Phys. Chem. Chem. Phys.*, vol. 14, no. 15, p. 5064, 2012.
- <sup>13</sup> M. Mantina, A. C. Chamberlin, R. Valero, C. J. Cramer, and D. G. Truhlar, “Consistent van der waals radii for the whole main group,” *J. Phys. Chem. A*, vol. 113, no. 19, pp. 5806–5812, 2009.
- <sup>14</sup> D. K. Owens, “Estimation of the surface free energy of polymers,” *Journal of Applied Polymer Physics*, vol. 13, p. 1741, 1969.
- <sup>15</sup> *Surface design: applications in bioscience and nanotechnology*, p. 471.
- <sup>16</sup> D. M. Silver and S. Wilson, “Special invariance properties of  $[n+1/n]$  pade approximants in rayleigh-schrodinger perturbation theory. ii. molecular interaction energies,” *Proc. R. Soc. Lond*, vol. 383, no. 1785, pp. 477–483, 1982.
- <sup>17</sup> R. Zwanzig, *Lectures in Theoretical Physics*, vol. 3. New York: Wiley Interscience, 1961.
- <sup>18</sup> H. Mori, “Transport, collective motion, and brownian motion,” *Prog. Theor. Phys.*, p. 423.
- <sup>19</sup> H. Mori, “A continued-fraction representation of the time-correlation functions,” *Prog. Theor. Phys.*, vol. 34, p. 423, 1965.

### VIII. APPENDIX

#### A. Tables

$T$ ( $K$ )	$A$	$B$	$C$	$D$	$R^2$
260	$1914 \pm 143$	$16.2 \pm 0.2$	$32 \pm 3$	$4.0 \pm 0.4$	0.994
360	$1068 \pm 6$	$25.6 \pm 0.1$	$14.0 \pm 0.2$	$1.64 \pm 0.05$	0.998

TABLE I: Gaussian fit parameters for the two primary maxima, at 260  $K$  and 360  $K$ .

$A$ ( $\times 10^{-3}$ )	$B$ ( $\times 10^{-3}$ )	$C$	$D$	$E$	$F$	$R^2$
$-6.11 \pm 0.06$	$-7.59 \pm 0.07$	$-2.2 \pm 0.1$	$0.94 \pm 0.01$	$1.11 \pm 0.01$	$52.8 \pm 0.7$	0.755

TABLE II: Paraboloid fitting parameters corresponding to Eq. 11.

Plane & Fit	$A$ ( $\times 10^{-3}$ )	$B$	$R^2$	$\theta_C$ ( $^\circ$ )
X=0 Left	$716.5 \pm 0.3$	$89.996 \pm 0.005$	0.999	$36.62 \pm 0.01$
X=0 Right	$718.1 \pm 0.3$	$181.75 \pm 0.04$	0.999	$35.68 \pm 0.01$
Y=0 Left	$644.0 \pm 0.3$	$93.667 \pm 0.004$	0.999	$32.78 \pm 0.01$
Y=0 Right	$-641.6 \pm 0.3$	$177.77 \pm 0.04$	0.999	$32.68 \pm 0.01$

TABLE III: Parabola fitting parameters and associated contact angle corresponding to Eq. 12.

Fig.	$A$ ( $\times 10^{-3}$ )	$B$ ( $\times 10^{-3}$ )	$C$ ( $\times 10^{-3}$ )	$D$ ( $\times 10^{-3}$ )	$E$ ( $\times 10^{-6}$ )	$F$	$R^2$
14(a)	$79 \pm 2$	$0.16 \pm 0.01$	$-0.99 \pm 0.03$	$-2.7 \pm 0.3$	-	-	0.999
14(b)	$20 \pm 195$	$0 \pm 2$	$-2 \pm 7$	$0.003 \pm 0.008$	$-6 \pm 1$	$10 \pm 4$	0.992
14(c)	$-29 \pm 205$	$1 \pm 2$	$7 \pm 7$	$0.010 \pm 0.007$	$-6.1 \pm 0.2$	$9.5 \pm 0.4$	0.965
14(d)	$214 \pm 155$	$1.1 \pm 0.4$	$2 \pm 2$	$-2 \pm 0.4$	-	-	0.965

TABLE IV: Surface energy Padé approximant fitting parameters corresponding to Eq. 8. The parameters are given in order beginning with the numerator, followed by the denominator.

$A$ ( $\times 10^{-20}$ )	$B$ ( $\times 10^{-22}$ )	$C$ ( $\times 10^{-25}$ )	$D$ ( $\times 10^{-3}$ )	$R^2$
$7 \pm 5$	$-4 \pm 3$	$6 \pm 6$	$2.4 \pm 3$	0.965

TABLE V: Mixing and cutting potential fitting parameters corresponding to Fig. 14(f).